

JGR Space Physics

RESEARCH ARTICLE

10.1029/2019JA026588

Key Points:

- We calculate ionospheric and field-aligned currents associated with the intra-D ring azimuthal fields observed on Cassini's proximal passes
- Ionospheric currents are 0.5–1.5 MA/rad similar to auroral values, while current densities are 5–10 nA/m² more than an order smaller
- Complex current patterns often show close north-south conjugacy on larger spatial scales consistent with a variable interhemispheric system

Correspondence to:

G. J. Hunt,
g.hunt@imperial.ac.uk

Citation:

Hunt, G. J., Cowley, S. W. H., Provan, G., Cao, H., Bunce, E. J., Dougherty, M. K., & Southwood, D. J. (2019). Currents associated with Saturn's intra-D ring azimuthal field perturbations. *Journal of Geophysical Research: Space Physics*, 124, 5675–5691. <https://doi.org/10.1029/2019JA026588>








Received 4 FEB 2019

Accepted 8 JUL 2019

Accepted article online 16 JUL 2019

Published online 30 JUL 2019

Currents Associated With Saturn's Intra-D Ring Azimuthal Field Perturbations

G.J. Hunt¹ , S.W.H. Cowley² , G. Provan² , H. Cao^{3,1,4} , E.J. Bunce² , M.K. Dougherty¹ , and D.J. Southwood¹ 

¹Blackett Laboratory, Imperial College London, London, UK, ²Department of Physics and Astronomy, University of Leicester, Leicester, UK, ³Department of Earth and Planetary Science, Harvard University, Cambridge, MA, USA, ⁴Division of Geological and Planetary Sciences, California Institute of Technology, Pasadena, CA, USA

Abstract During the final 22 full revolutions of the Cassini mission in 2017, the spacecraft passed at periapsis near the noon meridian through the gap between the inner edge of Saturn's D ring and the denser layers of the planet's atmosphere, revealing the presence of an unanticipated low-latitude current system via the associated azimuthal perturbation field peaking typically at ~10–30 nT. Assuming approximate axisymmetry, here we use the field data to calculate the associated horizontal meridional currents flowing in the ionosphere at the feet of the field lines traversed, together with the exterior field-aligned currents required by current continuity. We show that the ionospheric currents are typically ~0.5–1.5 MA per radian of azimuth, similar to auroral region currents, while the field-aligned current densities above the ionosphere are typically ~5–10 nA/m², more than an order less than auroral values. The principal factor involved in this difference is the ionospheric areas into which the currents map. While around a third of passes exhibit unidirectional currents flowing northward in the ionosphere closing southward along exterior field lines, many passes also display layers of reversed northward field-aligned current of comparable or larger magnitude in the region interior to the D ring, which may reverse sign again on the innermost field lines traversed. Overall, however, the currents generally show a high degree of north-south conjugacy indicative of an interhemispheric system, certainly on the larger overall spatial scales involved, if less so for the smaller-scale structures, possibly due to rapid temporal or local time variations.

1. Introduction

On the final 22 proximal orbits of the Cassini mission at Saturn between late April and mid-September 2017, corresponding to spacecraft revolutions (Revs) 271–292, the spacecraft passed through the equatorial plane near periapsis in the noon sector at variable altitudes between ~2,000 and ~4,000 km above the 1-bar atmospheric layer, in the narrow gap between the inner boundary of Saturn's ring system and the denser layers of the planet's atmosphere. The mission ended in the upper atmosphere pre-periapsis on Rev 293. An unanticipated feature of the magnetic data in the previously unexplored equatorial region is the presence of a distinctive signature in the azimuthal field component confined to field lines threading the tenuous inner D ring of the planet and field lines interior thereto, a region that we will term the intra-D ring region. The azimuthal field was usually positive in the sense of planetary rotation, a few tens of nanotesla in amplitude, and approximately symmetrical in form about the magnetic equator (Dougherty et al., 2018).

Such field perturbations are suggestive of the presence of an interhemispheric field-aligned current that usually flows north to south on and inside D ring field lines, which closes south to north in the region below the spacecraft, presumably in the Pedersen layer of the planetary ionosphere centered ~1,000 km above 1 bar (Galand et al., 2011). Estimates of the total current flowing suggest values ~0.25–1.5 MA per radian of azimuth (Dougherty et al., 2018), with a simple overall best-fit model constructed by Khurana et al. (2018) carrying a current of 1.15 MA/rad. Such currents are notably similar in magnitude to those flowing on auroral region field lines at northern and southern latitudes poleward of ~70° (Bradley et al., 2018; Hunt et al., 2014, 2015, 2018). However, the field lines on which these intra-D ring currents flow map to the ionosphere within ~30° of the equator in the north and within ~25° in the south, the north-south asymmetry being due principally to the strong quadrupole planetary field component.

Khurana et al. (2018) suggested that the currents are driven by shears in neutral atmospheric wind between the northern and southern ionospheric ends of the field lines, noting the strong latitudinal gradients in tropospheric wind associated with the equatorial jet (e.g., García-Melendo et al., 2011), combined with the above north-south asymmetry in ionospheric field line latitudes. Comparison of the currents involved with those in the auroral regions is not, therefore, intended to imply close commonality of physical origin.

While the papers by Dougherty et al. (2018) and Khurana et al. (2018) discuss the data from nine initial proximal passes, Revs 271–280, omitting Rev 277, a subsequent paper by Provan et al. (2019) has overviewed the data from all 23 proximal Revs, including final partial Rev 293. They showed that the azimuthal field profiles exhibit considerable pass to pass variability, including cases with intervals of strong negative azimuthal field, implying related variability in the strength and direction of the current flow. They also showed that the poloidal (B_r and B_θ) field components measured simultaneously display similar smoothly varying profiles pass to pass irrespective of the nature of the variable azimuthal field, with no evidently related variations on similar spatiotemporal scales (see Figures 2 and 3 of Provan et al., 2019). These findings thus support the picture suggested by Dougherty et al. (2018) and Khurana et al. (2018) that the azimuthal fields relate to an interhemispheric magnetosphere-ionosphere coupling current system which is at least somewhat azimuthally extended in nature but which is significantly temporally variable on proximal orbit period intervals of ~ 6.5 days. In this paper, we show that given this inference, it is possible to simply calculate the interhemispheric currents flowing in the meridian from the observed azimuthal field profiles and to estimate the associated current densities. Simple estimates of the total currents flowing were previously made on a related basis by Provan et al. (2019). Here we show that the horizontal meridional ionospheric currents and integrated field-aligned currents are typically ~ 0.5 – 1.5 MA/rad in magnitude, in conformity with previous approximate estimates, while newly showing that the associated field-aligned current densities are typically ~ 5 – 15 nA/m², both just above the ionosphere and at spacecraft altitudes. While the total current values are similar to those associated with the auroral currents, as previously pointed out by Dougherty et al. (2018) and Khurana et al. (2018), the current densities in the equatorial system are more than an order of magnitude lower. We elucidate the reasons for this difference.

2. Data Analysis Procedures

2.1. Observational and Theoretical Scenario

Observational and theoretical conditions related to this study are illustrated in Figure 1, where we show views of a meridian plane in cylindrical (ρ, z) coordinates, where ρ is perpendicular distance from the planetary spin/magnetic axis and z is distance along the axis from the equatorial plane positive northward. In both panels in Figure 1, the orange spheroid corresponds to the body of the planet shown extending to the ionospheric conducting layer $\sim 1,000$ km above the 1-bar surface, thus with polar and equatorial radii of 55,364 and 61,268 km, respectively. The arrowed black solid lines show the background field lines obtained by using the principal first three terms (dipole, quadrupole, and octupole) of the axisymmetric Dougherty et al. (2018) internal field model, plus the Bunce et al. (2007) ring current model for a nominal subsolar magnetopause radius of $22 R_S$. (R_S is Saturn's 1 bar equatorial radius equal to 60,268 km.) The darker blue area shows the field lines passing through the main ring region extending to $\sim 2.27 R_S$ in the equatorial plane (horizontal dotted line), corresponding to the outer boundary of the A ring. The lighter blue area shows the field lines passing through the innermost D ring at equatorial distances between 1.11 and $1.24 R_S$, on and inside of which (white area), the intra-D ring azimuthal field perturbations are observed.

In Figure 1a, the trajectories of two typical proximal Revs are shown projected into the meridian with the arrows indicating the direction of motion, from inbound in the northern hemisphere to outbound in the southern hemisphere. Specifically, we show the trajectories of Revs 287 (red) and 288 (blue) whose field data (amongst other Revs) are analyzed in section 3, representative of proximal Revs with larger and smaller perisapsides, respectively. The solid circles just north of the equator mark the points where the trajectories in the meridian lie tangent to the field lines, corresponding to the points where they map along field lines to the ionosphere closest to the equator, corresponding for Rev 287 to colatitudes from the northern pole of $\sim 72^\circ$ in the northern hemisphere and $\sim 98^\circ$ in the southern hemisphere and for Rev 288 to $\sim 76^\circ$ in the northern hemisphere and $\sim 94^\circ$ in the southern hemisphere. These points will be referred to below as the “field

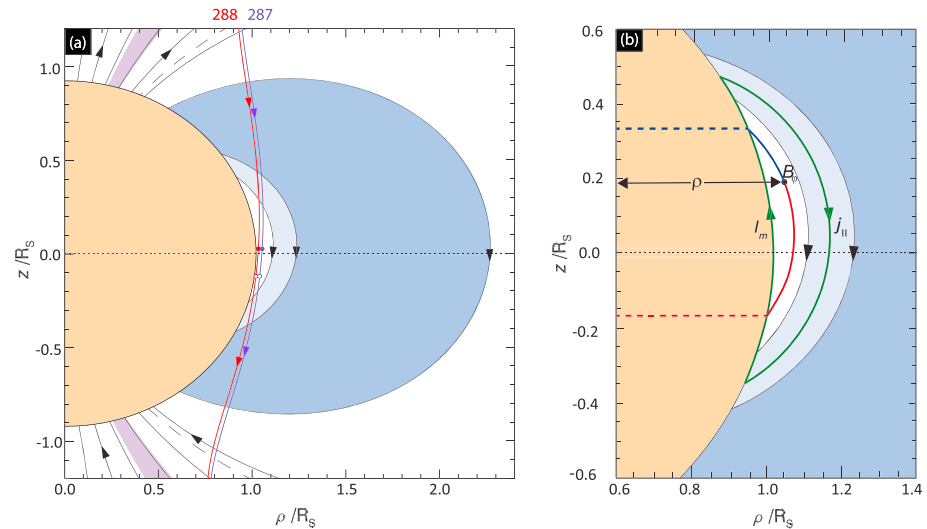


Figure 1. Plots of Saturn inner field line regimes in a meridian plane in cylindrical (ρ, z) coordinates, where ρ is the perpendicular distance from the spin/magnetic axis and z is distance along the axis positive northward. The outer edge of the planetary body (orange spheroid) is taken to be the main conducting ionospheric layer 1,000 km above the 1-bar reference spheroid, while the arrowed black lines show model field lines derived using the first three terms of the Dougherty et al. (2018) planetary field model plus the Bunce et al. (2007) ring current model for a typical subsolar magnetopause radius of $22 R_S$. The darker blue areas indicate field lines passing through the main ring region in the planet's equatorial plane (black dotted line), bounded by the field line passing through the outer boundary of the A ring. The lighter blue area corresponds to field lines passing through the innermost D ring. In Figure 1a, polar field lines have been drawn at 5° colatitude intervals from the southern pole between 0° and 30° , together with their northern conjugate counterparts, while the purple areas indicate the approximate conjugate locations of the main auroral field-aligned currents in both hemispheres. Cassini trajectories for Revs 287 (blue) and 288 (red) are shown projected into the meridian, representative of those with larger and smaller proximal periapsides. Spacecraft motion is from north to south. Small solid circles just north of the equator indicate the field parallel points where the trajectories in the meridian lie tangent to the field lines, corresponding to the points where they attain maximum mapped colatitudes (minimum mapped latitudes) in the ionosphere, while small open circles located south of the equator indicate the periapsis points. Figure 1b shows the region containing the D ring field lines in the same format but on an expanded scale. Arrowed green lines show the intra-D ring current system envisaged, consisting of a variable meridional ionospheric current, I_m , positive northward as shown, closed by an outer field-aligned current, $j_{||}$, positive southward along the background field as shown, resulting in an interior positive azimuthal perturbation field B_ϕ . The blue and red lines show cuts in the meridian through surfaces of revolution about the z axis that are employed in section 2.1 in the application of Ampère's circuital law to the observation of azimuthal field B_ϕ at the arbitrary intra-D ring point shown by the solid black circle. The solid portions of these lines follow field lines from the observation point to the conducting layer of the ionosphere, while the dashed portions complete the surface in some arbitrary manner through the body of the planet.

parallel" points on each pass, the concurrent eastward motion of the spacecraft from morning to afternoon local times (LTs) notwithstanding. The open circles south of the equator show the periapsis points, at radial distances of 1.047 and $1.027 R_S$ for Revs 287 and 288, respectively. The time spent on and inside main ring field lines on each pass was ~ 1 hr, of which the central ~ 28 min was located in the intra-D ring region, the latter spanning LTs between ~ 10.7 -hr inbound and ~ 12.4 -hr outbound on the passes shown.

The green lines in Figure 1b show the current system envisaged, consisting of a latitudinally variable meridional current I_m flowing in the ionosphere, taken positive northward, with current continuity maintained by distributed field-aligned currents, $j_{||}$, positive southward along the background field direction, confined to the intra-D ring region (light blue and white areas). These solenoidal currents then generate an azimuthal field B_ϕ within the intra-D ring region, positive in the sense of planetary rotation (into the plane of the diagram) for the sense of current flow depicted. We then consider the observation of azimuthal field B_ϕ at some arbitrary point inside the current region with perpendicular distance ρ from the planetary spin/magnetic axis, as shown by the small black circle. Assuming axisymmetry, Ampère's circuital law shows that the total current I^* passing through any surface bounded by an axial circle radius ρ passing through the point of measurement is given by

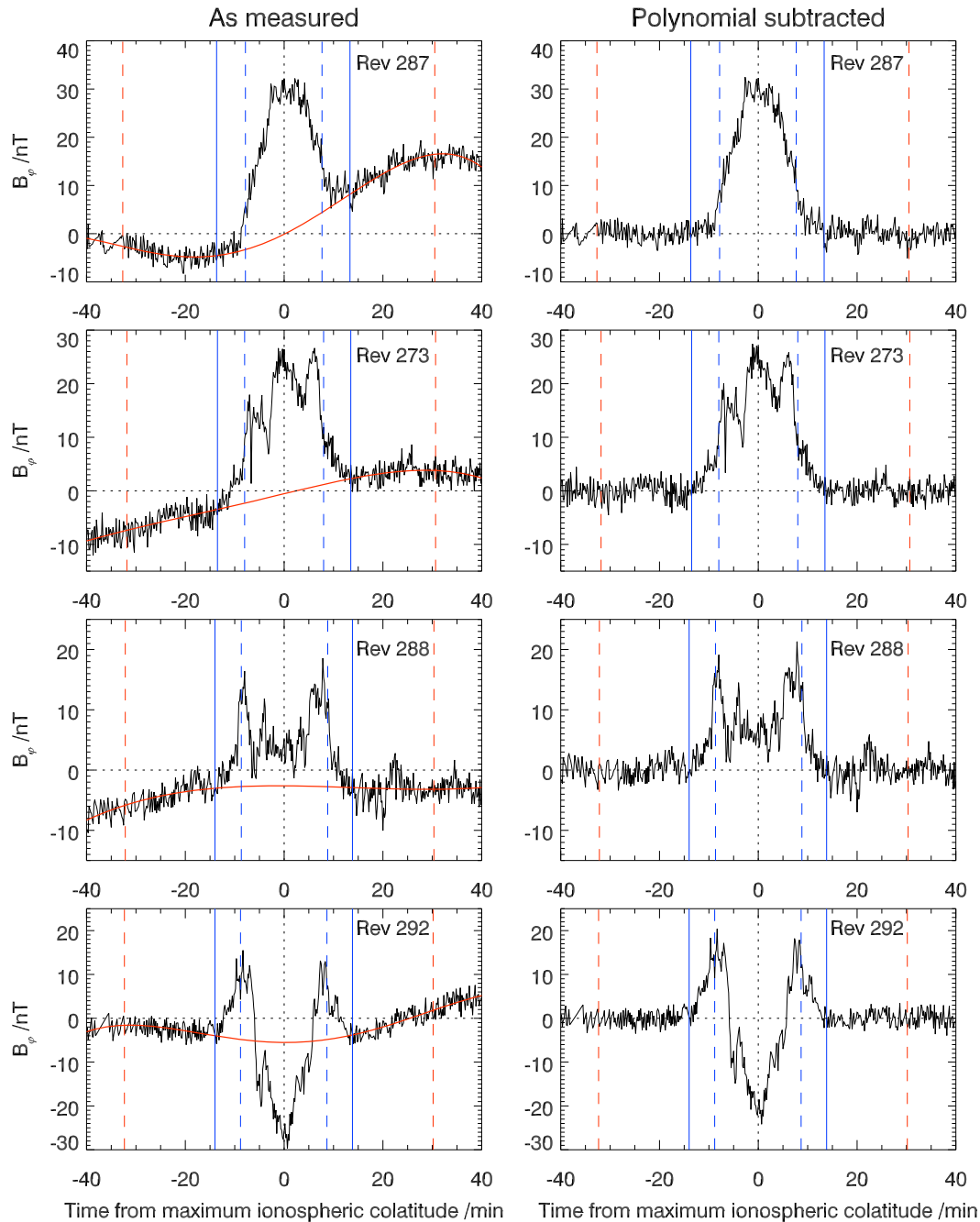


Figure 2. Plots showing the azimuthal field profiles of four representative proximal periaxis passes examined in detail in section 3, namely, category A pass 287, category B passes 273 and 288, and category U pass 292. Figures 2a–2d show the field as measured over a ± 40 -min interval centered on the field parallel point (vertical black dotted line) taken as $t = 0$, while Figures 2e–2h show the field with baseline removed. The baseline is formed from a fourth order polynomial fit to the data in Figures 2a–2d excluding the intra-D ring data. The UT times of the field parallel points are 17:18.5 UT (hr:min) on day 219 for Rev 287, 06:12.3 UT on day 129 for Rev 273, 04:18.2 UT on day 226 for Rev 288, and for 00:04.7 UT on day 252 Rev 292 (all 2017). The vertical lines indicate field lines passing through the equatorial plane at ring boundaries. The outer pair of red dashed lines correspond to the outer boundary of the A ring, while the inner pair of blue lines correspond to the outer (solid) and inner (dashed) D ring boundaries.

$$I^* = \frac{2\pi\rho B_\phi}{\mu_0}, \quad (1)$$

where μ_0 is the permeability of free space. In Figure 1b, we consider two such surfaces of revolution about the planetary axis, indicated in the meridian by the blue and red solid and dashed lines. These extend

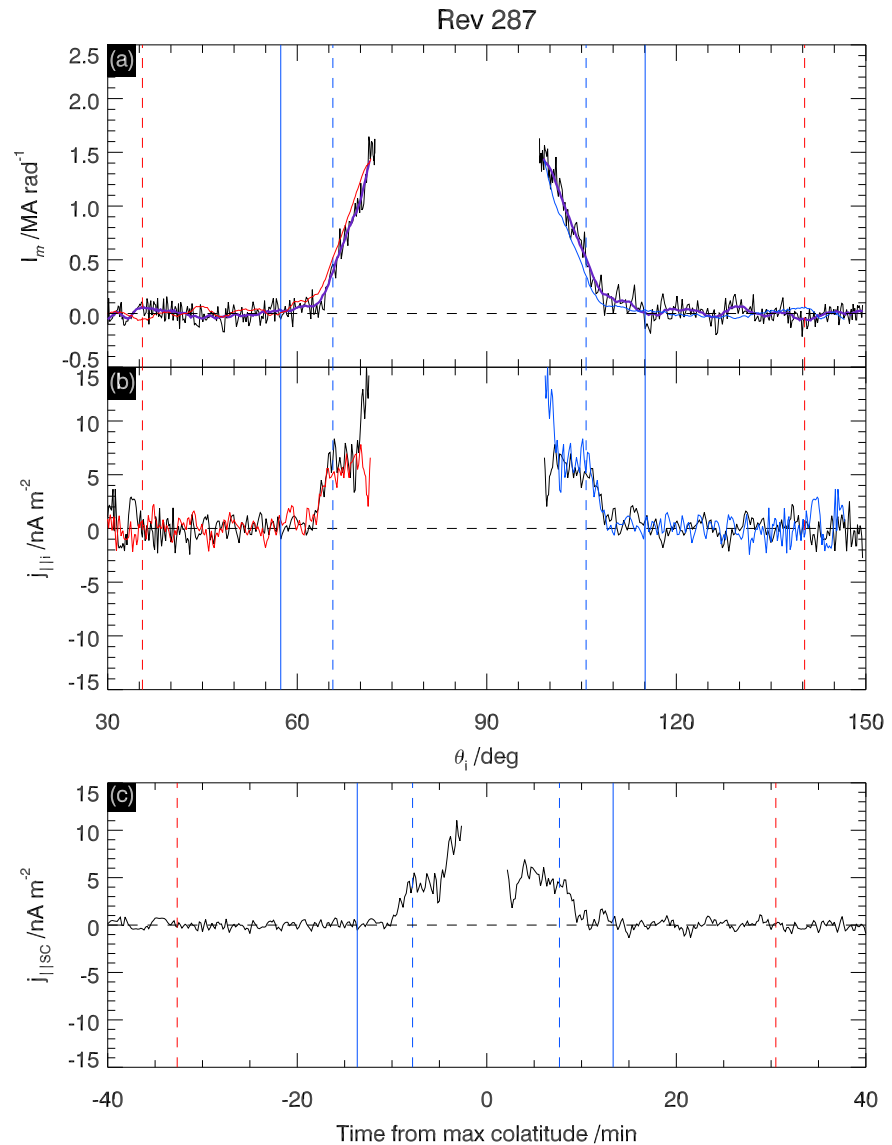


Figure 3. Ionospheric current per radian of azimuth and field-aligned current density profiles derived from the azimuthal magnetic field data shown in Figure 2e for category A Rev 287. As in Figure 2, the vertical lines indicate the locations/times where the magnetic field lines map to the outer edge of the A ring (red dashed lines) and the outer (blue solid lines) and inner (blue dashed lines) edges of the D ring. Figure 3a shows the ionospheric meridional current, I_m (MA/rad), positive northward, plotted versus ionospheric colatitude, θ_i (deg), measured from the northern pole. The black line shows the value calculated directly from the 10-s field data using equation (2), while the purple line shows the smoothed profile using a sliding 2.5-min window. The blue and red lines show the northern profile mapped along field lines into the southern hemisphere and the southern profile mapped along field lines to the northern hemisphere, respectively. In Figure 3b, the black line shows the field-aligned current density just above the conducting layer of the ionosphere, positive along the background field direction, calculated from the gradient of the smoothed ionospheric current profile using equation (3). The blue line shows the northern current density profile mapped along field lines into the southern hemisphere, while the red line shows the southern current density profile mapped into the northern hemisphere. Figure 3c shows the current density local to the spacecraft as a function of time relative to the field parallel point.

along the field lines from the point of observation to the ionosphere in the north and south as shown by the blue and red solid lines, respectively, and then pass through the body of the planet in some arbitrary manner indicated by the blue and red dashed lines. Since the current passing through these surfaces in their field-aligned portion (solid lines) is zero from the assumed geometry of the current system and since the net current flowing through them within the body of the planet inside of the ionosphere (dashed lines) must

also zero, the interior planetary currents forming a closed system, the total current flowing through these surfaces is just the meridional ionospheric current at the two ends of the field line, both north and south. Dividing by 2π , equation (1) shows that the meridional ionospheric current per radian of azimuth, positive northward, flowing at the feet of the field lines north and south are equal, and given by

$$I_m = \frac{\rho B_\phi}{\mu_0} \quad (2)$$

We note current continuity requires that the currents given by equations (1) and (2) are also equal to the total field-aligned currents flowing on intra-D ring field lines passing outside of the axial circle considered, as required by current continuity. This can be shown directly by alternatively applying Ampère's law to a surface bounded by the axial circle that instead passes outward across the full width of the intra-D ring field lines outside of the circle in Figure 1b, closing north or south over or through the planet outside of the intra-D ring field region.

The values of the field-aligned current density (nA/m^2) flowing on the field lines above the ionospheric layer can thus be determined from current continuity by considering the rate of change of I_m across the intra-D ring field lines. In Appendix A, we show that the associated field-aligned current density just above the ionosphere, positive southward along the background field, is given by

$$j_{\parallel i}(\theta_i) = \frac{n_r(\theta_i)}{R_i^2(\theta_i) \sin \theta_i} \left(\frac{B_i(\theta_i)}{B_{ni}(\theta_i)} \right) \frac{dI_m(\theta_i)}{d\theta_i} \quad (3)$$

where θ_i is the ionospheric colatitude of the spacecraft's magnetic foot point as measured from the north pole, $R_i(\theta_i)$ is the radial distance of the ionosphere from the planet's center taken to be a spheroid of revolution with equatorial and polar radii 1,000 km above the 1-bar surface as above, $n_r(\theta_i)$ is the radial component of the outward unit normal to the ionospheric surface, $B_i(\theta_i)$ is the ionospheric field strength, $B_{ni}(\theta_i)$ is the field normal to the ionospheric surface positive outward, and $I_m(\theta_i)$ positive northward is given by equation (2). From current continuity the current density at any other point (r, θ) on the same field line, in particular that at the spacecraft, is given by

$$j_{\parallel}(r, \theta) = \left(\frac{B(r, \theta)}{B_i(\theta_i)} \right) j_{\parallel i}(\theta_i) \quad (4)$$

In Appendix B, we show that equations (1)–(4) remain approximately valid if the solenoidal current structure is of finite azimuthal length or varies significantly with azimuth, provided that the azimuthal length scale concerned is somewhat larger than the dimensions in the meridian of the effective solenoid. If from Figure 1b, we take the latter dimension to be, for example, $\sim 0.25 R_S$, then we require the azimuthal length scale to be at least, for example, $\sim 0.5 R_S$, corresponding to ~ 2 hr of LT (see further in Appendix B). The data discussed by Provan et al. (2019) demonstrate directly from the LT coverage on each pass (~ 1.5 -hr LT) and over the proximal orbit data set as a whole (~ 3.5 -hr LT) that the corresponding structures are at least as azimuthally extended as this.

2.2. Data Set and Analysis Methodology

Figure 2 shows azimuthal field data from the four representative proximal periapsis passes analyzed in detail here, plotted over the interval ± 40 min about the time of the field parallel point taken as $t = 0$ (see Figure 1a). The UT times at this point are given in the figure caption. The 80-min interval shown encompasses the full pass across the ring region field lines as indicated by the set of vertical lines, the outer pair of red dashed lines corresponding to the field line passing through the outer boundary of the A ring, while the inner pair of blue lines similarly correspond to the field lines passing through the outer (solid) and inner (dashed) boundaries of the D ring. The fields as measured are plotted in Figures 2a–2d, clearly showing the intra-D ring field features, approximately symmetrical about the field parallel point, superposed on a more slowly varying ring region background. These data have been derived from measurements using the highest range of the flux-gate magnetometer for total field strengths above 10,000 nT, with digitization steps of 5.4 nT (Dougherty et al., 2004). They have been averaged here to 10-s resolution to reduce the corresponding digitization

noise to the few-nT level that remains evident, for example, in the region of more slowly varying fields outside of the D ring region.

Initial analysis of the data follows the methodology adopted by Provan et al. (2019). To isolate the main intra-D ring B_ϕ feature, we first fit a fourth order polynomial to the data over the interval shown but excluding the intra-D ring data between the middle pairs of blue dashed lines in the figure. These fits are shown by the red lines in Figures 2a–2d, taken to form an appropriate interpolated baseline for the measurements in the intra-D ring region. This baseline is subtracted from the azimuthal magnetic field data to yield the profiles shown in Figures 2e–2h, which are employed to derive the associated ionospheric meridional current per radian of azimuth at the feet of the field lines, I_m , using equation (2). We note with Provan et al. (2019) that since the perpendicular distance ρ remains near $\sim 1 R_S$ on these passes (Figure 1a), equation (2) may be approximated for rough estimates by $I_m \approx 0.048 B_\phi (nT)^{MA/rad}$, though the full formula is employed here. The currents are then projected to the ionosphere as a function of colatitude from the northern pole, θ_i , using the same field model as employed in Figure 1. The choice of subsolar magnetopause stand-off distance for the Bunce et al. (2007) ring current model has a negligible effect (less than 0.1°) on the determined colatitude as the field model is dominated by the planetary field close to the planet.

The field-aligned current density flowing immediately above the ionospheric conducting layer is then calculated from the meridional current profile using equation (3) and the current density at the spacecraft using equation (4). Since these quantities require estimation of the gradient of the meridional current with colatitude, the time series I_m data are first smoothed using a running average with a window width of 2.5 min, which removes the small-scale fluctuations while preserving the overall field structure and its gradients. We note that projection of the currents along field lines to the ionosphere inescapably leaves a “gap” in the ionospheric current profile across the equator corresponding to field lines that lie “beneath” the spacecraft trajectory that are not crossed during the pass. These cross-equatorial gaps are $\sim 25^\circ$ wide for passes with larger periapsides such as Rev 287, decreasing to $\sim 20^\circ$ wide for passes with smaller periapsides such as Rev 288. Small variations in the smoothed currents near the “ends” of this gap north and south, mapping to increasingly small latitudinal segments of the ionospheric layer, can also lead to sharp unphysical spikes in the estimated current density at these points. We have therefore imposed an empirically determined limit to the second derivative with respect to colatitude of the smoothed ionospheric current, related to the rate of change of the current density with colatitude through equation (3), which eliminates this effect. Specifically, we impose $d^2 I_m / d\theta_i^2 \leq 0.5$, with I_m in MA/rad and θ_i in degrees. This procedure widens the gap to $\sim 26^\circ$ for passes with larger periapsides, decreasing to $\sim 21^\circ$ for passes with smaller periapsides.

3. Results

We now present current and current density results as described above for four representative intra-D ring passes. Provan et al. (2019) have recently suggested a broad division of passes into four categories, though noting that the data generally display more a continuum of behaviors rather than completely distinct types. In essentially all cases, the field profiles show approximate symmetry about the magnetic equator, though differing in the number, form, and sign of the peaks in field observed. In category A, comprising $\sim 35\%$ of the passes (8 out of 23), the azimuthal field forms one central near-symmetric peak of magnitude ~ 20 – 40 nT, as indicated in the initial presentations of Dougherty et al. (2018) and Khurana et al. (2018). In category B, comprising a further $\sim 30\%$ of the passes (7 out of 23), the field has two near-symmetric peaks typically of smaller ~ 10 - to 20 -nT magnitude located near to or just inside of the inner D ring boundary field line, sometimes with a third peak of comparable magnitude centered near the field parallel point. In subcategory C, consisting of $\sim 15\%$ of the passes (3 out of 23), the peak fields remain of similar reduced magnitude but show irregular forms with significant asymmetries about the field parallel point. Finally, in category U passes, comprising $\sim 20\%$ of cases (5 out of 23) the fields have a well-defined near-symmetric profile but one which is unique within the proximal data set, including cases with negative azimuthal fields which are as strong as the positive fields in category A and B cases. Here we present analyses of data from category A pass Rev 287, category B passes Revs 273 and 288 with and without strong central maxima, and category U pass 292 which exhibits strong central negative fields. Asymmetric subcategory C passes are not fully amenable to the analysis outlined above which assumes approximate axisymmetry and are not examined further.

3.1. Rev 287

We begin by examining category A pass Rev 287, with results shown in Figure 3. As in Figure 2, the vertical lines indicate field lines that map to the outer boundary of the A ring and the outer and inner boundaries of the D ring. Figure 3a shows the ionospheric meridional current, I_m , positive northward, derived from the azimuthal field data in Figure 2e using equation (2) and mapped to the ionosphere using the model field employed in Figure 1 where it is plotted as a function of colatitude from the northern pole θ_i . The black line shows the current calculated from the 10-s data, while the purple line shows the smoothed profile using the 2.5-min sliding window as described in section 2.2. It can be seen that the smoothed profile appropriately removes the small-scale fluctuations while preserving the large-scale features. As indicated above, the central near-equatorial gap in the 10-s data corresponds to inner field lines not crossed on the spacecraft trajectory. It can be seen that the current begins to increase to positive values on D ring field lines both north and south and continues to increase near linearly with colatitude in the region inside the D ring, reaching peak values of ~ 1.5 MA/rad at the largest colatitudes reached, corresponding to $\sim 71^\circ$ in the northern hemisphere and $\sim 98^\circ$ in the southern hemisphere. This value is similar to those presented by Dougherty et al. (2018), Khurana et al. (2018), and Provan et al. (2019). It seems clear from this profile, however, that the current is still rising strongly with colatitude in the innermost part of the region sampled, with the actual peak northward current flowing across the equatorial region remaining undetermined. The truncated rise in azimuthal field values in the central region of the pass seen in Figures 2a and 2e is thus essentially a geometric effect as the spacecraft moves increasingly tangentially to the field lines.

To assess the degree of north-south symmetry of the current system, we have mapped the smoothed northern current profile into the southern hemisphere along model field lines, shown by the blue line in Figure 3a, and also the southern current profile into the northern hemisphere, shown by red lines. Comparing the red and blue profiles to the purple profiles in each hemisphere, it can be seen that the profiles are closely symmetrical, consistent with an interhemispheric field-aligned current flow. Any small departures from conjugacy could result from temporal, LT, or field model variations. However, the precise origin of these variations is beyond the focus of the present paper which is the currents' strength and density.

The positive gradient of the ionospheric current with colatitude in the northern hemisphere is indicative of an upward field-aligned current (flowing away from the ionosphere), while the negative gradient in the southern hemisphere indicates a downward field-aligned current (flowing toward the ionosphere). The corresponding field-aligned current densities just above the ionosphere derived using equation (3) are similarly shown versus northern colatitude in Figure 3b, where it can be seen that the currents rise from small values on central D ring field lines and plateau at positive values ~ 6 nA/m² near and just inside the inner D ring boundary in both hemispheres. As indicated in section 2.1 and Appendix A, positive values indicate field-aligned current flow in the same direction as the background field in both hemispheres, while negative values indicate current flow opposite to the field direction in both hemispheres. Thus, as required by the northward sense of the ionospheric current, the field-aligned currents flow away from the ionosphere in the northern hemisphere where the field points outward and toward the ionosphere in the southern hemisphere where the field points inward, that is, a north to south directed current flow along the field lines. The high degree of interhemispheric symmetry is again seen from mapping the northern current density profile along field lines into the southern hemisphere (blue line) and similarly the southern profile along field lines into the northern hemisphere (red lines). However, a further sharp increase in current density is derived from the northern ionospheric current profile near the largest colatitudes reached, not mirrored in the southern profile. This is due to a sudden small change in I_m occurring over a small range of colatitudes close to the edge of the main current.

Figure 3c shows the corresponding field-aligned current density local to the spacecraft, $j_{\parallel SC}$, derived using equation (4), shown as a function of time from the field parallel point. Due to the low altitude nature of the pass (radial distance $1.054 R_S$ at the field parallel point), the downscaling of the current density relative to the ionospheric value resulting from the relative field strengths is seen to be modest, with values plateauing at ~ 5 nA/m² just inside the D ring inner boundary.

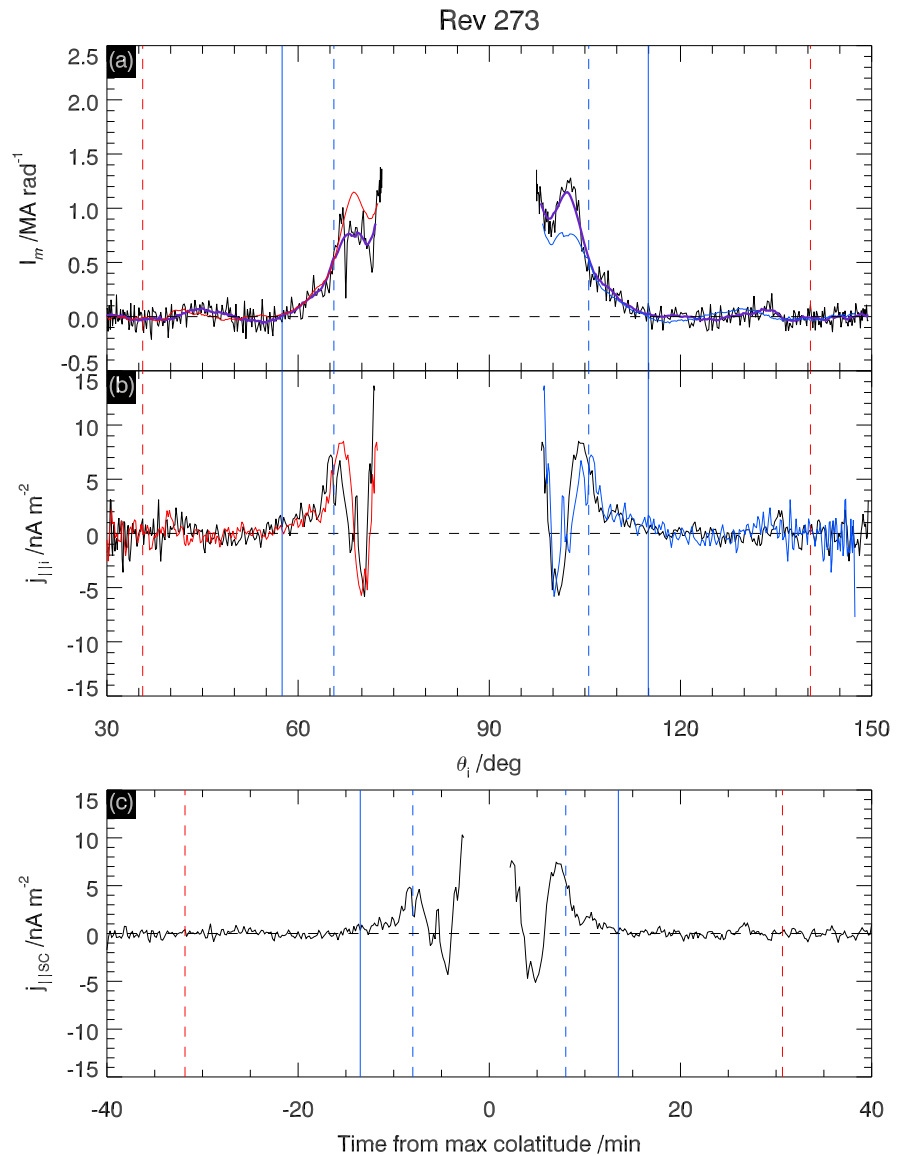


Figure 4. Ionospheric current and field-aligned current density profiles derived from the azimuthal magnetic field data shown in Figure 2f for category B Rev 273. The format is the same Figure 3.

3.2. Rev 273

In Figure 4, we present results for category B pass Rev 273, in the same format as Figure 3. As can be seen from Figure 2f, the azimuthal field on this pass has two well-defined peaks located just inside of the inner boundary of the D ring, together with a central field maximum of slightly larger magnitude. The mapped ionospheric current in Figure 4a correspondingly has two peaks just inside the inner D ring boundary, ~ 0.8 MA/rad at $\theta_i \approx 72^\circ$ in the northern hemisphere and moderately larger at ~ 1.1 MA/rad at $\theta_i \approx 102^\circ$ in the southern ionosphere. The red and blue mapped profiles show that these two features are closely conjugate but highlight the north-south difference in magnitude. The currents then increase once more to peak at ~ 1.3 MA/rad in the inner region. The strongly rising form of these inner currents again make it clear that the actual peak northward current flowing across the equatorial region remains undetermined.

We note that the reversal in the gradient of I_m across the peaks is indicative of a reversal in the direction of the field-aligned current from southward in the outer region mapping to the D ring to northward interior to the peaks. The field-aligned current then reverses sign again to southward as the meridional current

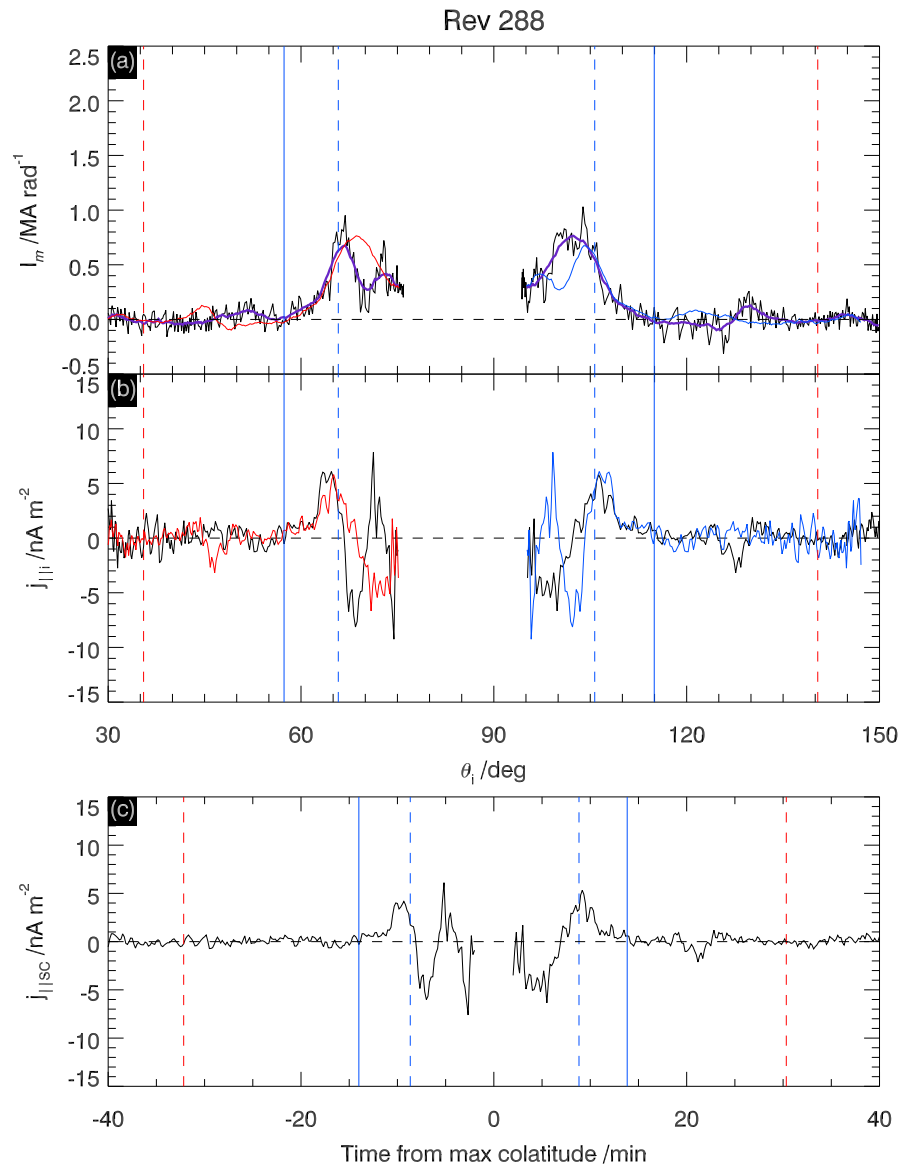


Figure 5. Ionospheric current and field-aligned current density profiles derived from the azimuthal magnetic field data shown in Figure 2g for category B Rev 288. The format is the same Figure 3.

subsequently increases once more toward its central peak. These variations are clearly seen in Figure 4b, where the ionospheric field-aligned current density initially rises from small positive values at the outer boundary of the D ring, directed from north to south along the background field, to a positive peak of $\sim 7\text{--}8\text{ nA/m}^2$ at or near the inner boundary of the D ring field line. The field-aligned current then near-conjugately reverses to a negative peak $\sim 5\text{ nA/m}^2$ inside of the inner D ring boundary, directed from south to north opposite to the background field, before reversing once more to a positive north to south value of $\sim 10\text{--}15\text{ nA/m}^2$ in the region of the central maximum. Once again, these features are reproduced in the current density at the spacecraft with only a small reduction in magnitude, as shown in Figure 4c.

3.3. Rev 288

In Figure 5, we show results for category B pass Rev 288, the general form of which is similar to Rev 273 in Figure 4. The azimuthal field in Figure 2g again has two positive peaks located just inside the D ring inner boundary field line, though of lesser magnitude than Rev 273 in Figure 2e, interior to which the fields

remain smaller and more irregular in form. The ionospheric current in Figure 5a shows corresponding behavior, with near-conjugate peaks of ~ 0.8 MA/rad lying just inside the inner boundary of the D ring but with variable currents differing north-south in the interior region, as shown by the red and blue mapped profiles. The corresponding ionospheric field-aligned currents in Figure 5b are positive on D ring field lines, rising to near-conjugate peaks of ~ 5 nA/m² just outside of the inner boundary of the D ring, before falling nonconjugately to negative values of ~ -5 nA/m² closer to the boundary in the northern hemisphere than in the southern, as is clear from comparison with the blue and red mapped profiles. The field-aligned currents in the northern hemisphere then show further nonconjugate reversals of a similar magnitude that are not present in the southern hemisphere, associated with a partially resolved small-scale meridional current (and azimuthal field) structure that is present in the northern hemisphere data but not in the southern (Figure 2g). These results in which field-aligned currents apparently flow in opposite directions along field lines in the northern and southern hemispheres might be taken as evidence of cross-field current flow in the region between. Alternatively, given the overall nature of the phenomenon it seems plausible that they are possibly due to few-minute fluctuations in the fields and currents on the time scale of the pass or to small-scale azimuthal variations in the currents given the ~ 1.7 -hr increase in LT across the noon meridian that occurred within the intra-D ring region or to variations in background magnetic field not captured by the planetary field model employed. It is important to note that only one other category B pass (Rev 284) shows a similar nonconjugacy.

3.4. Rev 292

In Figure 6, we show results for one of the more prominent “unique” cases, Rev 292, which exhibits a central negative azimuthal field, peaking near the field parallel point, whose magnitude is comparable to that of the central positive field peaks of the category A passes. As can be seen in Figure 2h, however, the field perturbations are initially positive starting on D region field lines, before peaking just inside the inner boundary of the D ring, and then falling to negative values in the interior region. A prominent field fluctuation is also seen in the northern hemisphere in the negative field regime, which is only partially marked at the corresponding position in the southern hemisphere. Figure 6a shows the ionospheric meridional current correspondingly rising near conjugately (shown by the red and blue lines) from small values at the outer boundary of the D ring to positive peaks of ~ 0.8 MA/rad just inside the inner D ring boundary, similar to Figures 4 and 5. However, the current then falls to negative (southward) values reaching ~ -1.2 MA/rad in the interior region. The current remains strongly falling with colatitude in the innermost region sampled, again indicating that the actual peak southward current flowing in the equatorial region, together with the peak negative azimuthal field, remains undetermined. The smaller-scale field fluctuations in the negative field region noted above are also seen to lead to significant inflections in the smoothed ionospheric current profiles in Figure 6a.

The field-aligned currents shown in Figure 6b peak at ~ 5 nA/m² near to or just outside of the inner boundary of D ring field lines, before falling near conjugately to strongly negative (northward) values in both hemispheres just inside the inner D ring boundary, with peak values of ~ -18 nA/m² in the northern hemisphere and ~ -10 nA/m² in the southern hemisphere. The current inflection associated with the small-scale field features (only partially resolved in the northern hemisphere) is associated with the calculated negative current density reducing near to zero near-conjugately in both hemispheres, before resuming comparably large ~ -15 to -20 nA/m values in the inner field region sampled.

4. Discussion

The analysis in section 3 shows that the integrated currents flowing in the intra-D ring current sheet are of typical magnitude ~ 0.5 – 1.5 MA/rad, consistent with the initial estimates of Dougherty et al. (2018), Khurana et al. (2018), and Provan et al. (2019). As these authors noted, such currents are comparable in magnitude to those flowing in the main current sheets at auroral latitudes (Bradley et al., 2018; Hunt et al., 2014, 2015, 2018). However, as also shown in section 3, the field-aligned current densities in the intra-D ring layers are typically ~ 5 – 10 nA/m², more than an order of magnitude smaller than the auroral current densities of typically ~ 50 – 150 nA/m² (e.g., Bunce et al., 2008; Hunt et al., 2014). We now briefly explore the origins of this difference by making some simple estimates.

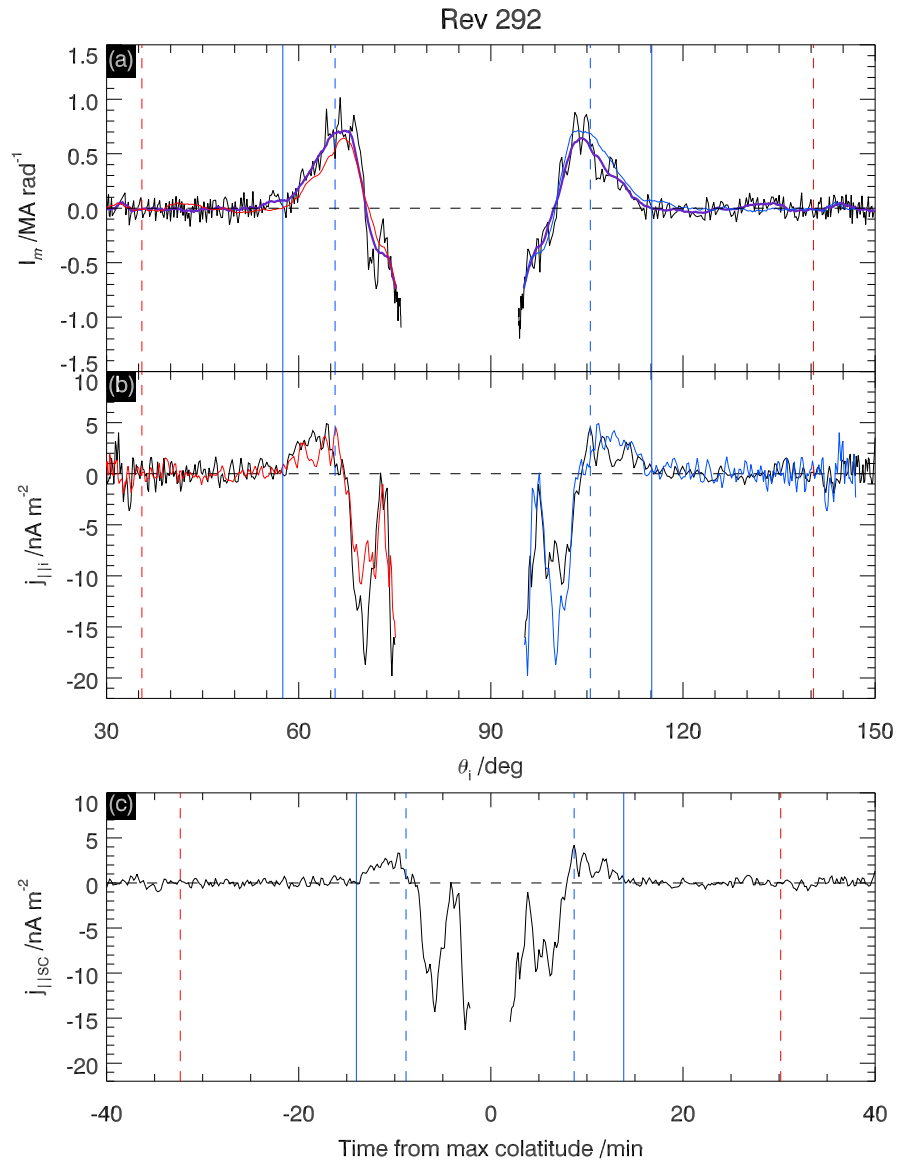


Figure 6. Ionospheric current and field-aligned current density profiles derived from the azimuthal magnetic field data shown in Figure 2h for category U Rev 292. The format is the same Figure 3.

For these purposes, we approximate equation (3) as

$$j_{\parallel i}(\theta_i) \approx \frac{1}{R_i^2(\theta_i) \sin \theta_i |\cos \alpha_i(\theta_i)|} \frac{\Delta I_m}{\Delta \theta_i}, \quad (5)$$

where ΔI_m is the total current per radian of azimuth flowing in the current sheet, $\Delta \theta_i$ is the ionospheric latitudinal width of the sheet, θ_i is taken as the center colatitude of the sheet, α_i is the angle of the ionospheric magnetic field to the ionospheric normal $\alpha_i(\theta_i) = \cos^{-1}(B_{n i}(\theta_i)/B_i(\theta_i))$, and we note that $n_r(\theta_i)$ in equation (3) is equal to unity to within less than 1% throughout.

We first consider the auroral current sheets, focusing specifically on the main upward current sheet associated with the auroral oval, whose properties observed in the near-midnight southern hemisphere on a sequence of Cassini orbits in 2008 are summarized in Table 2 of Hunt et al. (2014). Considering only the mean values in the table, we find $\Delta I_m \approx 2.7 \text{ MA/rad}$, $\Delta \theta_i \approx 1.7^\circ$, and colatitude from the southern pole $\theta_{iS} \approx 18^\circ$, such that $R_i \approx 55,855 \text{ km}$ (equation (A1)), and $|\cos \alpha_i| \approx 0.965$. Substitution into equation (5) yields

$j_{\parallel i} \approx 97 \text{ nA/m}^2$ in line with the above comments. The average over the individual current density estimates given by Hunt et al. (2014) is 128 nA/m^2 .

The results in section 3 then show that a typical equatorial current layer may be taken to be of strength $\sim 1 \text{ MA/rad}$, centered near the inner D ring field line boundary mapping in the northern ionosphere to northern colatitude $\sim 65.5^\circ$ and with a colatitudinal width of $\sim 5^\circ$ (spanning $\sim 1.08\text{--}1.14 R_S$ in the equatorial plane). The conjugate values in the southern ionosphere are a southern colatitude of $\sim 74.5^\circ$, with a width of $\sim 5.6^\circ$. The ionospheric radii are $\sim 60,113 \text{ km}$ in the north and $60,781 \text{ km}$ in the south, with field tilt angle factors $|\cos\alpha_i|$ of 0.444 in the north and 0.456 in the south. From equation (5), the estimated ionospheric current densities are then $\sim 8 \text{ nA/m}^2$ in the north and $\sim 6 \text{ nA/m}^2$ in the south, in line with the results in section 3 shown in Figures 3–6. These simple estimates thus yield equatorial current densities that are a factor ~ 15 smaller than corresponding auroral values.

Examining the terms that lead to this difference, we note that (a) the currents in the auroral sheets are typically larger than those in the equatorial sheets by a factor of ~ 3 , (b) the ionospheric latitudinal width of the auroral current layers are smaller than those of the equatorial current layers by a factor of ~ 3 , and (c) the ionospheric circumferential length per radian in the auroral region is smaller than that in the equatorial region by a factor of ~ 3 . Thus, the area into which the auroral currents map is an order of magnitude smaller than the area into which the equatorial currents map, and given the factor of ~ 3 enhancement of the total auroral current relative to the equatorial, these three factors would combine to make the auroral current density ~ 30 times the equatorial value. However, this factor is mitigated by the field tilt angle effect $|\cos\alpha_i|^{-1}$, which is a factor of ~ 2 larger for the equatorial current than for the auroral, so that the overall value is a factor of ~ 15 .

5. Summary and Conclusions

Following the initial reports of the presence of the intra-D ring azimuthal field perturbations from the early proximal orbit magnetic field data by Dougherty et al. (2018) and Khurana et al. (2018) and the first survey of all the proximal data by Provan et al. (2019), in this paper, we have examined the ionospheric meridional currents and related field-aligned current densities associated with the observed field signatures, assuming approximate local axisymmetry. We have shown (Appendix B) that the latter assumption requires the current structures to be at least $\sim 2\text{-hr}$ LT wide about the point of field measurement, which should usually be well satisfied given the observed systematics of the field data across $\sim 1.5\text{-hr}$ LT ranges on each pass, and across $\sim 3.5\text{-hr}$ LT about noon over the data set as a whole. We find on this basis that the horizontal ionospheric meridional currents are typically $\sim 0.5\text{--}1.5 \text{ MA/rad}$, while the associated field-aligned current densities in the intra-D ring layers are typically $\sim 5\text{--}10 \text{ nA/m}^2$. While the integrated meridional currents per radian of azimuth are thus comparable in strength to the auroral region currents, within a factor of ~ 3 , the associated field-aligned current densities just above the equatorial ionosphere are typically more than an order of magnitude lower than the field-aligned current densities just above the auroral ionosphere. We have shown that this is due to four factors, (a) the currents in the auroral layers are typical larger by a factor of ~ 3 , (b) the colatitudinal width of the auroral layers are smaller by a factor ~ 3 , (c) the ionospheric circumferential length per radian in the auroral region is smaller than that in the equatorial region by a factor of ~ 3 , leading overall to a factor of 30 , but (d) the field tilt angle effect is a factor of ~ 2 greater in the equatorial region compared to the auroral region leading to larger equatorial current densities than auroral by a factor 2 . The combined factor is thus ~ 15 larger for the auroral current densities above the ionosphere than for the near equatorial. Due to the low altitude of the proximal passes, the field-aligned currents at the spacecraft are similar to those just above the ionosphere.

As discussed previously by Provan et al. (2019), while $\sim 35\%$ of the passes (category A) are associated with a consistently northward directed ionospheric current peaking near the equator and a consistently southward directed field-aligned current flowing on and inside of D ring field lines as initially described, typically the currents have a more complex structure. In a further 30% of the passes (category B), for example, the field-aligned currents reverse to flow northward with comparable or larger magnitudes in narrower layers on field lines inside of the D ring interior to the outer southward currents and may or may not reverse sign again on the innermost field lines traversed. In many cases, the field and meridional current near the center of the pass peak in such a manner that it is clear that the actual peak fields and currents present on field

lines not traversed by the spacecraft could be significantly larger than those determined directly from the data, by factors of at least 2, if one extrapolates the I_m profiles to field lines “beyond” the spacecraft (see, e.g., Figures 3, 4, and 6). The “rounding” of field maxima observed across the equator in these cases is essentially a geometric effect caused by the spacecraft moving near tangentially along the current-carrying field lines.

While in this paper, we show two of the final five deepest orbits (Revs 288 and 292 periapsis altitudes at $\sim 1,700$ km above the 1-bar pressure surface); we conclude these signatures do not indicate dipping into the ionospheric current layer containing the south-north return current (I_m in Figure 1b). Our reasoning is as follows; the effect of this would be a reduction in the B_ϕ magnitude, down to zero if the spacecraft fully crossed the layer. It would not produce a reversal in B_ϕ underneath the ionospheric current layer. In addition, Provan et al. (2019) showed the azimuthal field signatures to be independent of periapsis altitude with equally variable signatures in the various altitude ranges (see their Table 1). This includes the category B signatures with a reduction of B_ϕ , these were observed at all altitude ranges. Furthermore, Hadid et al. (2018) showed the peak electron density to only be encountered on Cassini’s final plunge (Rev 293) at an altitude of $\sim 1,550$ km, some 200-km below the minimum altitude of Revs 288 and 292. Therefore, the peak of the ionospheric current layer was likely below the spacecraft on these Revs, too.

Generally, the currents show a high degree of north-south conjugacy consistent with the presence of an interhemispheric current system, certainly on the larger overall spatial scales involved. Khurana et al. (2018) have suggested this is driven by thermospheric azimuthal wind shears at the two ends of the field lines threading the intra-D ring region. If so, the overall results discussed above show that these wind shears must be highly variable in nature over the relatively short ~ 1 week pass to pass time scales. The issue of the origin of the pass to pass variability has previously been discussed by Provan et al. (2019), who showed no link could be detected to the altitude of the pass, the LT of the pass (~ 2 hr), the phases of the global Saturn planetary period oscillations, or the phase of the prominent asymmetry in Saturn ring structure associated with the D68 ringlet. The physical reason for the variability thus remains to be elucidated. However, the evidence points toward a significant role for variability in thermospheric winds, likely in combination with ionospheric conductivities (Hadid, Morooka, Wahlund, Moore, et al., 2018; Hadid et al., 2018; Wahlund et al., 2018), and possibly influenced by the variable inflow of $\sim 10^4$ kg/s of volatiles and dust into equatorial atmosphere (Hsu et al., 2018; Mitchell et al., 2018; Perry et al., 2018; Waite et al., 2018). Significant nonconjugacy in the field and current profiles is also often present on smaller spatial scales. These variations may possibly result from rapid temporal changes in the currents on the ~ 30 -min time scale of each intra-D ring pass. We note that the Alfvén bounce time is of the order of 4–5 s in this region; therefore, the time to reach Alfvénic equilibrium is much less than the time scale of the intra-D ring crossing. Additionally, azimuthal changes in the current structure over the ~ 1.5 -hr LT extent of each pass or variations in background magnetic field not captured by the field model employed in the ionospheric mapping could result in the variations.

Appendix A: Calculation of Ionospheric Current Density

The field-aligned current density just above the ionosphere associated with the intra-D ring current system is calculated from the colatitudinal variation of the northward ionospheric current $I_m(\theta_i)$ given by equation (2) assuming axisymmetry. The limitations imposed by the axisymmetric assumption are explored in Appendix B. The ionosphere is taken to be located at 1,000-km above the 1 bar radius, thus at equatorial and polar radii of $R_{e\ i} = 61,268$ km and $R_{p\ i} = 55,364$ km, respectively. The ionospheric radial distance at colatitude θ_i is then given by the spheroidal surface

$$R_i(\theta_i) = \frac{R_{e\ i}}{(1 + \varepsilon \cos^2 \theta_i)^{1/2}}, \quad (\text{A1})$$

with

$$\varepsilon = \left(\frac{R_{e\ i}}{R_{p\ i}} \right)^2 - 1 \quad (\text{A2})$$

From current continuity the current density normal to the ionospheric surface $j_{n\ i}(\theta_i)$, taken positive directed outward from the surface, satisfies

$$j_{n\ i}(\theta_i)R_i(\theta_i)\sin\theta_i\ ds = I_m(\theta_i + d\theta_i) - I_m(\theta_i) = dI_m, \quad (\text{A3})$$

where $I_m(\theta_i)$ is given by equation (2), ds is the element of length along the ionosphere in the meridian between θ_i and $\theta_i + d\theta_i$ given by

$$ds = \frac{R_i(\theta_i)d\theta_i}{n_r(\theta_i)}, \quad (\text{A4})$$

where $n_r(\theta_i)$ is the radial component of the outward unit normal to the surface given by equations (A1) and (A2). This unit normal is given by

$$\hat{n}(\theta_i) = n_r(\theta_i)\hat{r} + n_\theta(\theta_i)\hat{\theta} = \frac{[(1 + \varepsilon \cos^2\theta_i)\hat{r} - (\varepsilon \sin\theta_i \cos\theta_i)\hat{\theta}]}{[(1 + \varepsilon \cos^2\theta_i)^2 + (\varepsilon \sin\theta_i \cos\theta_i)^2]^{1/2}}. \quad (\text{A5})$$

From equations (A3) and (A4), we then have

$$j_{n\ i}(\theta_i) = \frac{n_r(\theta_i)}{R_i^2(\theta_i)\sin\theta_i} \frac{dI_m}{d\theta_i}. \quad (\text{A6})$$

The field-aligned current density just above the ionosphere is then given by

$$j_{\parallel\ i}(\theta_i) = \left(\frac{B_i(\theta_i)}{B_{n\ i}(\theta_i)} \right) j_{n\ i}(\theta_i) = \frac{n_r(\theta_i)}{R_i^2(\theta_i)\sin\theta_i} \left(\frac{B_i(\theta_i)}{B_{n\ i}(\theta_i)} \right) \frac{dI_m}{d\theta_i}, \quad (\text{A7})$$

where $B_i(\theta_i)$ is the field strength in the ionosphere and $B_{n\ i}(\theta_i)$ is the normal component positive outward. We note that with these definitions of $j_{n\ i}(\theta_i)$ and $B_{n\ i}(\theta_i)$, both positive outward from the ionosphere, the field-aligned current density $j_{\parallel\ i}(\theta_i)$ as defined by equation (A7) is positive when directed parallel to the ionospheric field and negative when antiparallel, in both hemispheres. From current continuity, the local field-aligned current density at any other point (r, θ) along these field lines, including the point of observation, is then given by

$$j_{\parallel} = \left(\frac{B(r, \theta)}{B_i(\theta_i)} \right) j_{\parallel\ i}(\theta_i), \quad (\text{A8})$$

where $j_{\parallel\ i}(\theta_i)$ and $B_i(\theta_i)$ are the ionospheric field-aligned current density and ionospheric field strength at the feet of the field line at either end.

Appendix B: Limitations of the Axisymmetric Current Assumption

In this appendix, we explore the limitations on the validity of equations (2) and (3) if the current system illustrated in Figure 1b is not exactly axisymmetric. To do this, we assume instead that the effective solenoid is of azimuthal length L given approximately by

$$L \approx R_S \Delta\varphi, \quad (\text{B1})$$

where R_S is Saturn's 1 bar equatorial radius (60,268 km) and $\Delta\varphi$ is the azimuthal extent of the current system. We first note with Provan et al. (2019) that while the azimuthal field inside the solenoid may be somewhat variable in magnitude, associated with varying currents, it is nevertheless (with one exception shown in Figure 2h) generally unidirectional, positive in the sense of planetary rotation. Then the magnetic flux within the solenoid is given by

$$\Phi = \bar{B}_\varphi A \approx \bar{B}_\varphi Z \Delta\rho \quad (\text{B2})$$

where \bar{B}_φ is the mean (positive) azimuthal field within cross-sectional area A of the solenoid, the area being given approximately by the product of Z , the north-south extent of the solenoid, and $\Delta\rho$ its cylindrical radial

width. From Figure 1b, it can be seen that we may take $Z \approx 0.4 R_S$ and $\Delta\rho \approx 0.1 R_S$, given that the flux lies principally interior to the D ring field lines. At the ends of the solenoid, however, this flux spreads out into the exterior region to close around the solenoid in the usual quasidipolar pattern, in principle extending to infinity, but with the flux being confined principally to surrounding distances of order $\sim L$, at least above the ionosphere. We thus estimate the perturbation field strength outside of the solenoid b as

$$b \approx \frac{\Phi}{L^2} \approx \frac{\bar{B}_\varphi Z \Delta\rho}{L^2} \quad (\text{B3})$$

We then consider applying Ampère's law to the perimeter of a surface whose section in the meridian is again shown by either the red or blue lines in Figure 1b but is of finite azimuthal extent $\Delta\varphi$ given by the azimuthal extent of the solenoidal current. We take the azimuthal field within the solenoid, that is, at the small black circle in Figure 1b, to have some particular value B_φ , related to the mean field \bar{B}_φ by $B_\varphi = f\bar{B}_\varphi$, where over most of the area $f \sim 1$. The contribution to the line integral of \mathbf{B} on the circular segment inside the solenoid is $\mathcal{I}_1 \approx B_\varphi L$, while now in general we also have equal contributions from the two field-aligned portions of the path on either side of the solenoid of length $\Delta z \approx Z/2$, which will thus sum to be of order $\mathcal{I}_2 \approx 2b\Delta z \approx bZ$. The net contributions from inside the planet remain zero. For a given current per radian of azimuth within the azimuthal sector $\Delta\varphi$, the validity of equation (2) thus requires that \mathcal{I}_1 is large compared with \mathcal{I}_2 , that is, we require $B_\varphi L > bZ$. Introducing b from equation (B3) then gives the geometric condition

$$L^3 \gg \frac{Z^2 \Delta\rho}{f}, \quad (\text{B4})$$

that is, the length L must be sufficiently large compared with the transverse dimensions of the solenoid or

$$L > \sqrt[3]{\frac{Z^2 \Delta\rho}{f}} \quad (\text{B5})$$

We note that if L exceeds the right-hand side of equation (B5) by at least a factor of 2, this is sufficient to give at least an order of magnitude difference in the condition in equation (B4), given the cubic power on the left side. Since $\sqrt[3]{f}$ will generally be close to unity over nearly all of the area of interest, it is sufficient to consider $f = 1$ in equation (B5). Introducing the dimensions for Z and $\Delta\rho$ given above into equation (B4) then gives $\sqrt[3]{Z^2 \Delta\rho} \approx 0.25 R_S$. Thus, as a simple estimate we require $L \geq 0.5 R_S$ as a lower bound for the approximate validity of equation (2). This corresponds to $\sim 30^\circ$ of longitude around the planet, or ~ 2 hr of LT. We know from direct observation on individual passes that the effective length of the solenoid is generally at least ~ 1.5 hr, while over the proximal orbits as a whole, such field structures have been directly observed over ~ 3.5 hr of LT, from ~ 10 -hr prenoon to ~ 13.5 -hr LT post noon. It thus seems entirely plausible that conditions under which equation (2) is valid are generally maintained in the Saturn system.

Acknowledgments

Work at Imperial College was supported by STFC grant ST/N000692/1. Work at the University of Leicester was supported by STFC grant ST/N000749/1. E. J. B. is supported by a Royal Society Wolfson Research Merit Award. M. K. D. is funded by Royal Society Research Professorship RP140004. H. C. is funded by the Cassini project through NASA Jet Propulsion Laboratory contract 1579625. We thank Steve Kellock and the Cassini magnetometer team at Imperial College for access to processed magnetic field data. Calibrated magnetic field data from the Cassini mission are available from the NASA Planetary Data System at the Jet Propulsion Laboratory (<https://pds.jpl.nasa.gov/>).

References

- Bradley, T. J., Cowley, S. W. H., Provan, G., Hunt, G. J., Bunce, E. J., Wharton, S. J., et al. (2018). Field-aligned currents in Saturn's nightside magnetosphere: Subcorotation and planetary period oscillation components during northern spring. *Journal of Geophysical Research: Space Physics*, 123, 3602–3636. <https://doi.org/10.1002/2017JA024885>
- Bunce, E. J., Arridge, C. S., Clarke, J. T., Coates, A. J., Cowley, S. W. H., Dougherty, M. K., et al. (2008). Origins of Saturn's aurora: Simultaneous observations by Cassini and the Hubble Space Telescope. *Journal of Geophysical Research*, 113, A09209. <https://doi.org/10.1029/2008JA013257>
- Bunce, E. J., Cowley, S. W. H., Alexeev, I. I., Arridge, C. S., Dougherty, M. K., Nichols, J. D., & Russell, C. T. (2007). Cassini observations of the variation of Saturn's ring current parameters with system size. *Journal of Geophysical Research*, 112, A10202. <https://doi.org/10.1029/2007JA012275>
- Dougherty, M. K., Cao, H., Khurana, K. K., Hunt, G. J., Provan, G., Kellock, S., et al. (2018). Saturn's magnetic field revealed by Cassini's Grand Finale. *Science*, 362(6410). <https://doi.org/10.1126/science.aat5434>
- Dougherty, M. K., Kellock, S., Southwood, D. J., Balogh, A., Smith, E. J., Tsurutani, B. T., et al. (2004). The Cassini magnetic field investigation. *Space Science Reviews*, 114(1-4), 331–383. <https://doi.org/10.1007/s11214-004-1432-2>
- Galand, M., Moore, L., Mueller-Wodarg, I., Mendillo, M., & Miller, S. (2011). Response of Saturn's auroral ionosphere to electron precipitation: Electron density, electron temperature, and electrical conductivity. *Journal of Geophysical Research*, 116, A09306. <https://doi.org/10.1029/2010JA016412>

- García-Melendo, E., Péres-Hoyos, S., Sánchez-Lavega, A., & Hueso, R. (2011). Saturn's zonal wind profile in 2004–2009 from Cassini ISS images and its long-term variability. *Icarus*, 215(1), 62–74. <https://doi.org/10.1016/j.icarus.2011.07.005>
- Hadid, L. Z., Morooka, M. W., Wahlund, J.-E., Moore, L., Cravens, T. E., Hedman, M. M., et al. (2018). Ring shadowing effects on Saturn's ionosphere: Implications for ring opacity and plasma transport. *Geophysical Research Letters*, 45, 10,084–10,092. <https://doi.org/10.1029/2018GL079150>
- Hadid, L. Z., Morooka, M. W., Wahlund, J.-E., Persoon, A. M., Andrews, D. J., Shebanits, O., et al. (2018). Saturn's ionosphere: Electron density altitude profiles and D ring interaction from the Cassini Grand Finale. *Geophysical Research Letters*, 45. <https://doi.org/10.1029/2018GL078004>
- Hsu, H.-W., Schmidt, J., Kempf, S., Postberg, F., Moragas-Klostermeyer, G., Seif, M., et al. (2018). In situ collection of dust grains falling from Saturn's rings into its atmosphere. *Science*, 362(6410), eaat3185. <https://doi.org/10.1126/science.aat3185>
- Hunt, G. J., Cowley, S. W. H., Provan, G., Bunce, E. J., Alexeev, I. I., Belenkaya, E. S., et al. (2014). Field-aligned currents in Saturn's southern nightside magnetosphere: Sub-corotation and planetary period oscillation components. *Journal of Geophysical Research: Space Physics*, 119, 9847–9899. <https://doi.org/10.1002/2014JA020506>
- Hunt, G. J., Cowley, S. W. H., Provan, G., Bunce, E. J., Alexeev, I. I., Belenkaya, E. S., et al. (2015). Field-aligned currents in Saturn's northern nightside magnetosphere: Evidence for inter-hemispheric current flow associated with planetary period oscillations. *Journal of Geophysical Research: Space Physics*, 120, 7552–7584. <https://doi.org/10.1002/2015JA021454>
- Hunt, G. J., Provan, G., Bunce, E. J., Cowley, S. W. H., Dougherty, M. K., & Southwood, D. J. (2018). Field-aligned currents in Saturn's magnetosphere: Observations from the F-ring orbits. *Journal of Geophysical Research: Space Physics*, 123, 3806–3821. <https://doi.org/10.1002/2017JA025067>
- Khurana, K. K., Dougherty, M. K., Provan, G., Hunt, G. J., Kivelson, M. G., Cowley, S. W. H., et al. (2018). Discovery of atmospheric-wind-driven electric currents in Saturn's magnetosphere in the gap between Saturn and its rings. *Geophysical Research Letters*, 45, 10,068–10,074. <https://doi.org/10.1029/2018GL078256>
- Mitchell, D. G., Perry, M. E., Hamilton, D. C., Westlake, J. H., Kollmann, P., Smith, H. T., et al. (2018). Dust grains fall from Saturn's D-ring into its equatorial upper atmosphere. *Science*, 362(6410), eaat2236. <https://doi.org/10.1126/science.aat2236>
- Perry, M. E., Waite, J. H. Jr., Mitchell, D. G., Miller, K. E., Cravens, T. E., Perryman, R. S., et al. (2018). Material flux from the rings of Saturn into its atmosphere. *Geophysical Research Letters*, 45, 10,093–10,100. <https://doi.org/10.1029/2018GL078575>
- Provan, G., Cowley, S. W. H., Bunce, E. J., Bradley, T. J., Hunt, G. J., Cao, H., & Dougherty, M. K. (2019). Variability of intra-D ring azimuthal magnetic field profiles observed on Cassini's proximal periapsis passes. *Journal of Geophysical Research: Space Physics*, 124, 379–404. <https://doi.org/10.1029/2018JA026121>
- Wahlund, J.-E., Morooka, M. W., Hadid, L. Z., Persoon, A. M., Farrell, W. M., Gurnett, D. A., et al. (2018). In situ measurements of Saturn's ionosphere show that it is dynamic and interacts with the rings. *Science*, 359(6371), 66–68. <https://doi.org/10.1126/science.aao4134>
- Waite, J. H. Jr., Perryman, R. S., Perry, M. E., Miller, K. E., Bell, J., Cravens, T. E., et al. (2018). Chemical interactions between Saturn's atmosphere and its rings. *Science*, 362(6410), eaat2382. <https://doi.org/10.1126/science.aat2382>